Chapter 7. Formation, structure and dynamics of solar and stellar coronae and winds

https://doi.org/10.1017/S1743921320001441 Published online by Cambridge University Press

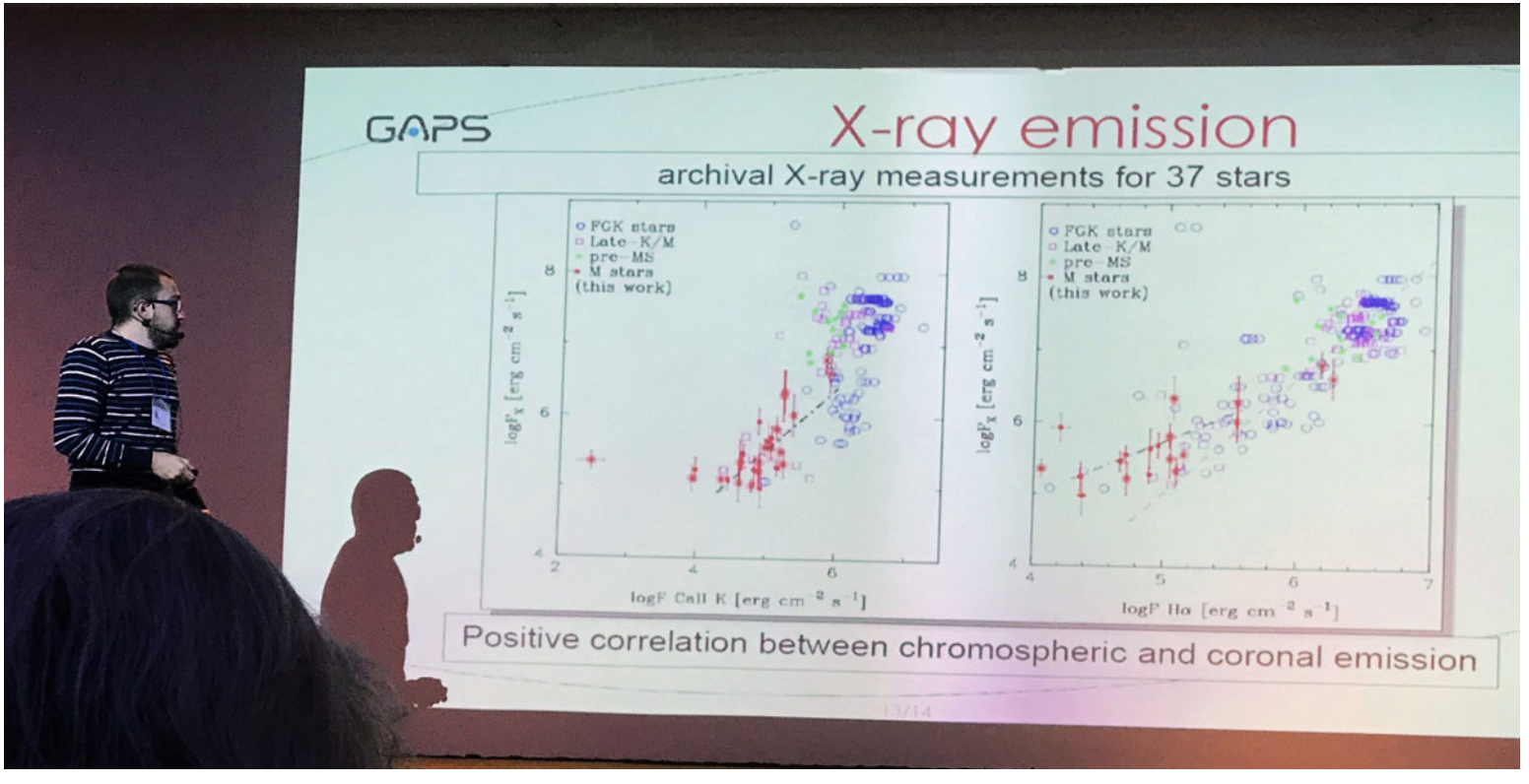

Gaetano Scandariato

Solar and Stellar Magnetic Fields: Origins and Manifestations
Proceedings IAU Symposium No. 354, 2019
A. Kosovichev, K. Strassmeier & M. Jardine, ed.
doi:10.1017/S1743921320001441

Observational constraints for solar-type Stellar winds

Manuel Güdel

University of Vienna, Department of Astrophysics
Türkenschanzstr. 17, 1180 Vienna, Austria
email: manuel.guedel@univie.ac.at

Abstract. Ionized winds from late-type main-sequence stars are important for stellar spin-down and therefore the evolution of stellar activity; winds blow an "astrosphere" into the interstellar medium that absorbs a large part of galactic cosmic rays; and the winds play a key role in shaping planetary environments, in particular their upper atmospheres. These issues have been well studied for the solar wind but little is known about winds escaping from other solar-type stars. Several methods have been devised to either detect winds directly or to infer the presence of such winds from features that are shaped by the winds. This paper summarizes these methods and discusses exemplary findings. There is need for more studies using multiple methods for the same stars.

Keywords. stars: winds, outflows; stars: rotation; radio continuum: stars; ultraviolet: stars

1. Introduction

The solar wind and by analogy ionized winds from cool main-sequence stars matter for many aspects of stellar and planetary evolution. Some of the most important roles of stellar winds are:

- Stellar braking and spin-down due to angular momentum removal by magnetized winds;
- Erosion of planetary atmospheres due to their interactions with stellar winds;
- Chemical processing of planetary atmospheres due to high-energy particles transported in the wind;
- Potential influence on the stellar luminosity evolution as the stellar mass may significantly decrease with time;
- Protection from a large part of galactic cosmic ray flux.

The solar wind, although directly accessible only since the beginning of the space age, is relatively well studied out to its limits at around 120 au where it is terminated in the region of interaction with the interstellar medium. Nevertheless, many aspects of the solar wind require further study, in particular,

- the heating and wind acceleration mechanism(s);
- the heating/cooling behavior across the heliosphere;
- the long-term evolution of the wind mass-loss rate which is possibly related to the magnetic dynamo operation and therefore rotation.

The solar wind is studied both *in situ* and remotely, e.g. using optical observations. In contrast, observing winds from cool main-sequence stars has turned out to be extremely difficult. In essentially all wavelength ranges, the emission from the star outshines the wind emission by far. Wind emission from far outside the stellar surface or absorption effects induced by the wind may be alternative ways to detect stellar mass loss.

On the other hand, *indirect* methods have been developed that observe easily accessible features around the star that are controlled by the wind, but that are not themselves part of the wind. Such methods have been more successful in estimating wind mass-loss rates although they often depend on assumptions and complex models linking the unobserved wind to the observed features.

This paper summarizes a variety of stellar-wind detection methods and presents results from corresponding observations. Only detection methods that can presently be applied to observations and that have provided useful results are discussed here. I do not aim to discuss wind physics beyond what is of immediate relevance to the models; nor do I intend to be comprehensive in presenting a review of all published results. For some methods, in particular those inferring wind mass loss from stellar spin-down, separate comprehensive reviews have been presented elsewhere.

2. Evidence for Winds from Stellar Spin-Down

The most fundamental evidence for the presence of ionized stellar winds is stellar spin-down. Spin-down is well documented by large surveys of rotation periods as a function of age (e.g., Irwin *et al.* 2011). Stars spin down because magnetic fields immersed in the wind plasma act as a lever arm on the stellar surface. A packet of mass leaving the stellar surface and moving out along a magnetic field line gains angular momentum as long as the field lines drag the gas mass and build up magnetic stresses, which is until it reaches the Alfvén surface (or Alfvén distance) where the Alfvén velocity drops below the wind speed and the gas drags the magnetic fields. Effectively, the angular momentum gained by reaching the Alfvén distance is extracted at the stellar surface, thus spinning down the star. This is a simplified sketch for a more gradual change from the magnetic-field dominated subalfvénic inner region to the superalfvénically expanding wind region (for an early theoretical model of angular momentum transport in a rotating solar wind, see Weber & Davis 1967).

A vast amount of literature has accumulated over the past several decades about many aspects of spin-down, angular momentum transfer from the star to the wind, and surveys of rotational evolution and rotation period distributions at given ages. I do not intend to review any of these topics here but summarize a few key findings before focusing on the spin-down evolution of a cool main-sequence star, exemplified by one model that focuses on this specific aspect rather than the reconstruction of all the underlying physical mechanisms (e.g., core-envelope decoupling, wind acceleration, torque formulae for magnetized flows, etc.).

The reality of a solar wind was recognized after extensive theoretical and predictive work by Parker (1958) and evidence provided by cometary tails (Biermann 1951), and finally *in situ* observations by space probes around 1960. The theoretical and observational basis to generalize winds to other stars was rapidly developed in (among others) three key papers I mention here briefly. In 1967, Kraft found that the average rotational velocities of stars with strong Ca II emission are higher than for weak Ca emitters. Because strong Ca II emitters were known to be younger, Kraft suggested that stars spin down with age, making magnetically coupled winds like the solar wind responsible for the angular momentum loss (Kraft 1967). He also recognized that this picture should apply to stars with outer convection zones. In the same year, Weber & Davis (1967) developed a theoretical model for the angular momentum transfer via magnetic wind torques. And in 1972, Skumanich summarized the observational aspects in a key paper (Skumanich 1972, 1.5 pages of text, 1 figure, 10 references) that laid the foundations of subsequent stellar statistical studies of age, evolution of activity, and rotation. He claimed that Ca II emission declines with the inverse square root of the age, and the same should hold for the rotation velocity. Given the proportionality between surface magnetic field strength

https://doi.org/10.1017/S1743921320001441 Published online by Cambridge University Press

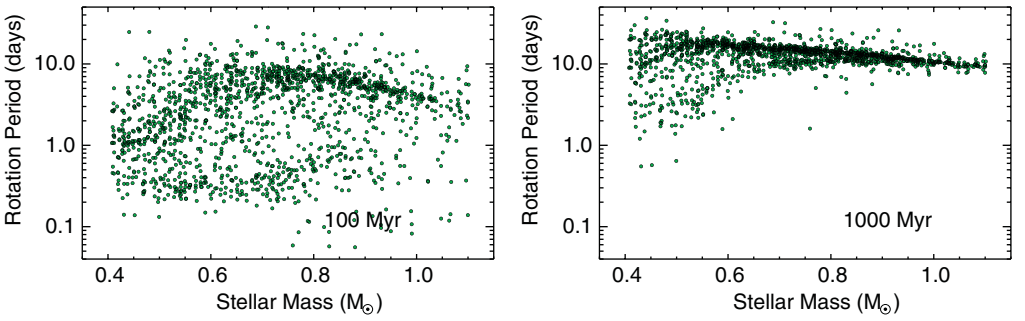

Figure 1. Snapshots of the rotation period distribution evolving in time. Rotation periods of a sample of ∼1500 observed stars from clusters with known ages have been used to develop a spin-down/wind/rotation evolution model. These same stars can then be evolved forward and backward in time. Shown here are two snapshots for ages of 100 Myr (left) and 1 Gyr (right). (From Johnstone *et al.* 2015.)

and Ca II emission, the magnetic fields are also supposed to decay with the inverse square root of the age. While we now know that corrections are needed in this rough picture, age-rotation-activity relations have been a focus in open cluster studies ever since.

Models of stellar rotational evolution have been developed by many groups, for the purpose of studying basic physical concepts and test them with observations (e.g., Gallet & Bouvier 2013), or for the purpose of reproducing phenomenologically the long-term evolution of stellar rotation. To conceptually describe the relevant model steps, I confine myself to one example model that comprises many relevant aspects, published by Johnstone *et al.* (2015).

Large observational samples from open clusters have shown a wide spread of rotation periods P for any given mass back to very early evolutionary stages, essentially starting in the T Tauri phase already. While the stars spin up during the pre-main sequence phase due to contraction, they spin down during their main-sequence life but still keep their wide spread in P until, at around 0.5–1 Gyr, most of them converge to a unique rotation period only depending on age and stellar mass (Soderblom *et al.* 1993; Fig. 1). This *convergence* is ascribed to a feedback between angular momentum removal by a magnetized coronal wind and the rotationally induced operation of an internal dynamo that generates the magnetic fields. Given that magnetized and ionized winds appear to be related to stellar coronae, one suspects that they, like other magnetic activity indicators, also decline with time. The goal then is to use the observed rotational evolution to derive the evolution of the wind mass-loss rate $\dot{M}$, even if the evolutionary tracks $P(t)$ are non-unique given the widely dispersed initial conditions.

The basic ingredients of a rotational evolution model are the initial rotation rate, the internal structure of the star, and the rate at which angular momentum is removed from the star by the wind. Rotational models also include core-envelope decoupling. This is relevant when the time scale for angular momentum transport within the star is significant compared to the time scale over which the moment of inertia of the star changes and the time scale over which angular momentum is removed from the stellar surface by the wind. Due to this mechanism, stars arriving on the Zero-Age Main-Sequence (ZAMS) have cores that rotate more rapidly than the surfaces.

We now need a set of equations to solve for the angular rotation rate $\Omega_*(t)$, the wind mass-loss rate $\dot{M}(t)$, and the surface magnetic field $B(t)$. Spin-down occurs because the rotating magnetic field transfers angular momentum to the wind flow that therefore removes it from the stellar surface. A numerical recipe therefore needs a formula for the

https://doi.org/10.1017/S1743921320001441 Published online by Cambridge University Press

torques that act on the star, and these torques τ are a function of stellar mass M_*, radius R_*, $\dot{M}$, B, and Ω_*,

$$\tau = f(B, \dot{M}, M_*, R_*, \Omega_*) \approx B^{0.87} \dot{M}^{0.56} R_*^{2.87} \Omega_* \tag{2.1}$$

where the numerical example on the right-hand side is simplified from a torque formula given by Matt *et al.* (2012). Such torque formulae are derived from simulations using some assumptions about the magnetic-field structure. The torque is required in the spin-down formula,

$$\frac{\mathrm{d}\Omega_*}{\mathrm{d}t} = \frac{1}{I_*} \left(\tau - \frac{\mathrm{d}I_*}{\mathrm{d}t} \right) \Omega_*, \tag{2.2}$$

where I_* is the star's moment of inertia derived from stellar structure models; we assume a dependency of $\dot{M}$ on R_*, Ω_*, and M_*,

$$\dot{M} = \dot{M}_\odot \left(\frac{R_*}{R_\odot} \right)^2 \left(\frac{\Omega_*}{\Omega_\odot} \right)^a \left(\frac{M_*}{M_\odot} \right)^b \tag{2.3}$$

where the exponents a and b will be fitted to observational constraints. We further need an equation for, in the simplest case, the equatorial magnetic field strength of the dominant dipole component,

$$B = B_\odot \left(\frac{\Omega_* \tau_*}{\Omega_\odot \tau_\odot} \right)^{1.32} \tag{2.4}$$

(Vidotto *et al.* 2014); τ_* is the convective turnover time of the star. We need to also consider that B "saturates" for rapidly rotating stars, i.e., is no longer a function of Ω. By implication, $\dot{M}$ should also saturate, as do many magnetic activity indicators such as the X-ray luminosity. The onset of saturation should be described by an equation like

$$\Omega_{\rm sat}(M_*) = \Omega_{\rm sat}(M_\odot) \left(\frac{M_*}{M_\odot} \right)^c \tag{2.5}$$

where c is a further fit parameter, and $\Omega_{\rm sat}(M_\odot) \approx 15 \Omega_\odot$. Equations (2.1)–(2.5) can be solved with fits to observations of rotation period distributions for a given mass at different ages. The evolutionary tracks $\Omega(t)$ and $\dot{M}(t)$ will depend on the initial condition $\Omega(t_0)$ taken from observed Ω distributions.

The results of this wind treatment are rotational evolution tracks and wind mass-loss tracks. The constants a, b, and c are 1.33, –3.36, and 2.3 in Johnstone *et al.* (2015). Examples of results are shown in Fig. 2. The rotational evolution of solar-mass stars converges to a unique age-dependent value after ∼700 Myr, while at 100 Myrs of age rotation periods are distributed over more than an oder of magnitude (between the 10th and the 90th percentiles). For stars older than ∼ 700 Myr, the mass-loss rate declines roughly as

$$\dot{M} \propto t^{-0.75}, \tag{2.6}$$

t being the age. The mass-loss rate is also related to the rotation period as

$$\dot{M} \propto R_*^2 \; M_*^{-3.36} \; \Omega_*^{1.33} \tag{2.7}$$

showing that the mass-loss rate decreases strongly with stellar mass but increases with rotation velocity; the saturation mass-loss rate is

$$\dot{M}_{\rm sat} = 37 \dot{M}_\odot \left(\frac{M_*}{M_\odot} \right)^{1.3}, \tag{2.8}$$

which means that higher-mass stars can achieve higher mass-loss rates. Saturation of $\dot{M}$ limits the mass-loss rates of young, very rapid rotators, as shown in Fig. 2.

https://doi.org/10.1017/S1743921320001441 Published online by Cambridge University Press

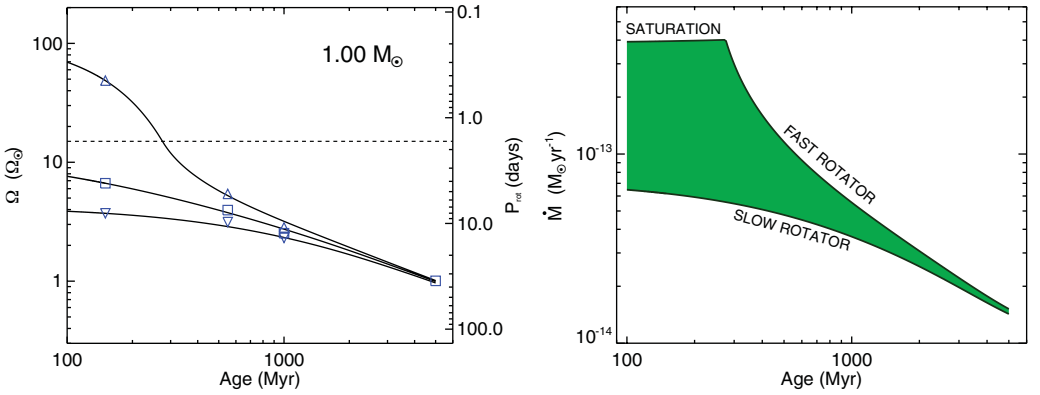

Figure 2. *Left:* Modeled rotational evolution of stars at the 10th, 50th, and 90th percentiles of the rotational distribution from 100 Myr to 5 Gyr. The blue symbols mark the same percentiles from observational distributions. The dashed line indicates the limiting rotation rate above which the wind mass-loss rate and the surface magnetic field saturate. – *Right*: The evolution of the solar wind mass loss rate with age on the main sequence. The green area includes all possible $\dot{M}$ evolutionary tracks for different initial rotation periods between the 10th percentile (bottom edge) and the 90th percentile (top edge). The fastest rotators remain saturated at a maximum $\dot{M}$ level during the first 300 Myr. (From Johnstone *et al.* 2015.)

For solar-type stars younger than ~ 700 Myr, the $\dot{M}$ history is non-unique and depends on the initial rotation period of the star. The result in Fig. 2-right shows that $\dot{M}$ of solar analogs is distributed over nearly an order of magnitude (10th to 90th percentile, green area) near the Zero-Age Main-Sequence (ZAMS) age, due to a broad distribution of initial rotation periods. Similar results were reported for lower-mass stars by Johnstone *et al.* (2015).

Specific wind models can be developed for individual stars if enough information is available about the stellar magnetic field and the stellar fundamental properties such as the rotation period. Vidotto *et al.* (2011b) developed a 3-D magnetohydrodynamic coronal-wind model using an observed stellar surface magnetic-field map for the M dwarf V374 Peg, and also applying magnetocentrifugal forces. The winds in this simulation reach final velocities of $(1500-2300)n_{12}^{-1/2}$ km s^{-1}, n_{12} being the coronal base density in units of 10^{12} cm^{-3}. The mass-loss rate then is $\dot{M} = 4 \times 10^{-10}\ n_{12}^{-1/2} M_\odot$ yr^{-1} where the corresponding angular momentum loss suggests that $n_{12} \lesssim 0.1$.

3. Hydrogen Walls and Lyα Absorption

The solar wind blows an ionized "bubble" into the surrounding interstellar medium (ISM), known as the heliosphere. The heliosphere interacts with the interstellar medium across three boundaries. At the termination shock, the supersonically expanding stellar wind decelerates to a subsonic flow. The (variable) location of the termination shock is known from measurements made by Voyager 1 and 2 that found it to lie at 94 au and 84 au, respectively (Stone *et al.* 2008), from the Sun, in different but roughly upstream directions as seen from the Sun. Further out, at approximately 120 au for both Voyagers (Stone *et al.* 2019), the heliopause separates the solar wind from the flow of the interstellar medium. Still further away from the Sun, a bow shock could develop in the interstellar medium where the flow changes from supersonic to subsonic. This depends on the relative velocity between the Sun and the ISM, and recent measurements show that the motion is subsonic and therefore no bow shock should form (McComas *et al.* 2012).

https://doi.org/10.1017/S1743921320001441 Published online by Cambridge University Press

If the ISM contains a neutral component – as is the case in the local ISM around the heliosphere – the neutral particles can penetrate into the heliosphere where they may undergo charge exchange (CX) reactions (see Sect. 4). A hot hydrogen wall builds up outside the heliopause absorbing significantly in the Lyα line. The same mechanism supposedly also occurs around nearby stars, and it is the observation of Lyα absorption from the *stellar* hydrogen wall that is the basis of an indirect method to quantify *stellar winds*, as largely worked out by B. Wood and colleagues (see review by Wood 2004 that guided the summary of this present section).

The method relies on a very accurate analysis of the line profile of the Lyα lines from H I and D I at ∼1216 Å. The usually very strong Lyα emission line is formed in the stellar chromosphere, but is also subject to strong absorption by neutral H in the interstellar medium, leading to complete absorption in the line center while only the line wings are accessible to observation. In contrast, the D I absorption line is displaced blueward from the H I line by 0.33 Å and is easily detected on the H I line wings. Observations of these profiles for the α Cen system showed a discrepancy in that the H I absorption revealed excess broadening and redshift by 2.2 km s^{-1} relative to D I (Linsky & Wood 1996). The excess was attributed to the presence of a relatively small column of hot neutral hydrogen (temperature of 30,000 K) around the equivalent of a heliosphere around α Cen, i.e., a neutral hydrogen wall around α Cen's "astrosphere", but the excess should also be influenced by the heliospheric H wall.

The heliospheric H wall produces excess absorption on the red side of the Lyα ISM absorption profile because the H wall material moves slower relative to the Sun than the ISM that imprints the ISM Lyα absorption profile. Conversely, the astrospheric excess absorption acts on the blue side of the Lyα absorption.

To make progress, the neutral H walls need to be related to the the helio-/astrospheres and therefore to solar and stellar winds by means of hydrodynamic simulations. Gayley *et al.* (1997) showed that the red excess absorption is consistent with heliospheric models. Further sightlines provide more absorption data that are reasonably well explained by a heliospheric model, opening up the possibility to infer ISM properties from the observations. However, results for the ISM are strongly model dependent considering the various regions of charge exchange in a multi-fluid or kinetic approach.

Analogously, the Lyα excess absorption from the astrospheric H wall is due to the presence of a stellar wind, and fluid or kinetic models can be used to quantify the stellar mass loss. To do so, the ISM flow must be determined in the rest frame of the star. Then, the wind mass-loss rates of the star are varied in the simulations until the excess absorption is well fitted. This then leads to an estimate of the stellar mass-loss rate, $\dot{M}$.

The Lyα absorption method has so far provided an appreciable number of indirect wind mass-loss estimates for a variety of stars, as summarized recently by Wood (2018). Before summarizing the systematics in the measurements of $\dot{M}$, I will mention some caveats of the method (see Wood 2018):

• Results depend on accurate numerical models of the highly complex interaction between the partly neutral ISM and the stellar (and solar) wind. However, models can be calibrated with the well studied *solar* wind.

• The local ISM properties around the target stars need to be sufficiently well understood; variations between nearby stars are deemed to be modest, however.

• The wind speeds are assumed to be solar in all models. This may be related to similar escape speeds for the observed stars, values that are similar to wind speeds, although rapidly rotating stars may eject much faster winds due to magneto-centrifugal acceleration (Holzwarth & Jardine 2007).

• The method applies only if the ISM around the target star is partially neutral. Absence of excess absorption may therefore not signify a weak wind but could be due to

https://doi.org/10.1017/S1743921320001441 Published online by Cambridge University Press

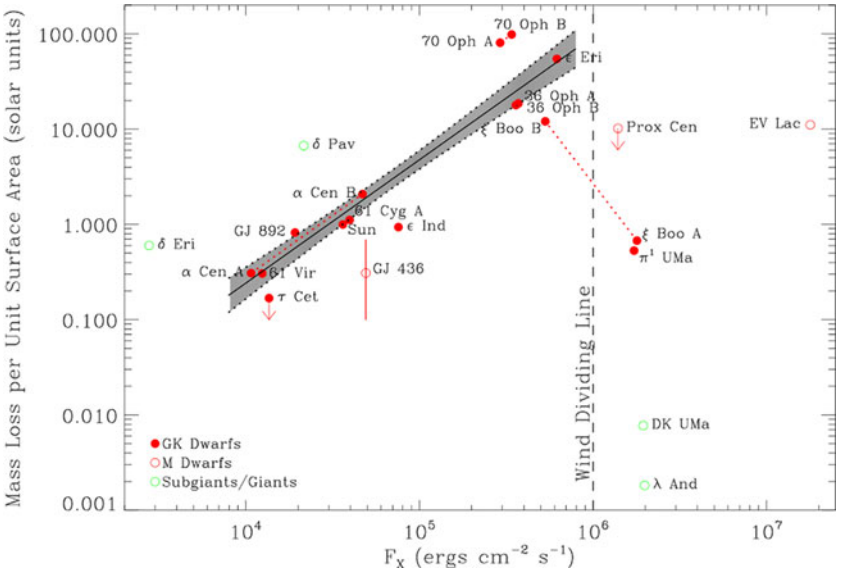

Figure 3. Stellar mass-loss rates per unit surface area as a function of the measured surface X-ray flux. The red filled, red open, and and green open circles mark main-sequence G&K stars, M dwarfs, and evolved stars, respectively. The gray band is a power-law fit with the uncertainty range for the main-sequence stars up to a maximum surface X-ray flux of 8×10^5 erg cm^{-2}s^{-1}. (From Wood 2018.)

the absence of a astrospheric hydrogen wall. Wood (2018) reports that within 7 pc of the Sun, most stars show excess absorption, while the percentage of detections drops rapidly beyond ~ 10 pc, indicating that the ISM at such distances is fully ionized.

- High ISM absorption may obscure the astrospheric excess absorption completely.
- Low ISM velocity relative to the star leads to cooler and less decelerated astrospheric H I, making the absorption narrower and difficult to separate from the ISM absorption.
- Very high ISM velocities, instead, may compress the astrosphere and heat the H wall sufficiently to make Lyα optically thin, complicating the interpretation further.

Despite some of the above caveats, the results do show important systematics. It is reasonable to correlate $\dot{M}$ with a stellar coronal activity parameter because the winds originate in the coronal region of a star, where magnetic fields are open rather than closed as in active regions. Plotting inferred stellar mass loss rates per stellar surface unit area against the average X-ray surface flux F_X (Fig. 3) finds the best-fit relation

$$\dot{M} \propto F_X^{1.34 \pm 0.18} \tag{3.1}$$

(Wood *et al.* 2005). This relation applies to G and K-type main-sequence stars with F_X up to about 20 times the solar F_X; for higher activity levels, $\dot{M}$ seems to be much lower than the extrapolated trend. There are some caveats here, however. Two of the detections among these very active objects are giants, and two more are small M dwarfs. The two active G/K targets that support very low $\dot{M}$ are ξ Boo A+B, a binary for which a precise separation of the contribution of A or B is not possible.

If the breakdown of $\dot{M}$ toward very active stars is real, an explanation may be sought in the magnetic field topology of the corona, e.g., dipolar magnetic fields anchored in large polar spots, inhibiting stellar winds (Wood 2018). This is problematic, however, in the light of strong spin-down exactly in the age range where active stars abound, i.e., for

https://doi.org/10.1017/S1743921320001441 Published online by Cambridge University Press

ages of 0.1–1 Gyr for solar analogs. Spin-down requires sufficiently strong $\dot{M}$ as discussed in Sect. 2; in fact, $\dot{M}$ correlates with Ω to achieve the observed rotational distributions,

$$\dot{M} \propto \Omega^{1.33}. \tag{3.2}$$

(see Eq. 2.7). Knowing the relation between $\dot{M}$ and activity, the evolution of $\dot{M}$ could be inferred if there were an age-activity relation. Relations reported by Ayres (1997) for the equatorial rotational velocity $v_{\rm rot}$,

$$v_{\rm rot} \propto t^{-0.6\pm0.1} \tag{3.3}$$

$$F_{\rm X} \propto v_{\rm rot}^{2.9\pm0.3} \tag{3.4}$$

can be used with Eq. (3.1) to infer

$$\dot{M} \propto t^{-2.33\pm0.55}. \tag{3.5}$$

Because of the breakdown of Eq. (3.1) for the most active stars, Eq. (3.5) applies only for ages greater than ∼700 Myr for solar analogs. I note here that for younger solar-type stars there is no useful age-activity relation like Eq. (3.3) because the spin-down history and therefore the rotational velocity history as well as the $F_{\rm X}$ history depend on (widely distributed) initial conditions, making gyrochronology and activity-age relations invalid at such ages (Johnstone *et al.* 2015; Tu *et al.* 2015; Sect. 2). The results above imply that at ∼700 Myr of age for a solar analog, the wind mass-loss rate is about a factor of 100 higher than in the present-day Sun.

Note also the anomalously low data point for GJ 436, an M3 dwarf for which, however, absorption by an evaporating planetary atmosphere was used (see Sect. 9 below). Together with the M dwarfs above the "Wind Dividing Line" at $F_{\rm X} = 10^6$ erg cm^{-2} s^{-1}, this may be an indication for generally weaker winds from M dwarfs, perhaps again related to the large-scale structure of the stellar magnetic field.

4. Astrospheric Charge Exchange

The solar wind can be subject to charge exchange (CX) as has been observed around comets (Lisse *et al.* 1996; Cravens 1997). In this process, a highly charged solar wind ion interacts with a neutral atom or molecule from the comet. Charge exchange can also occur between ions although this process is inefficient. Charge exchange populates levels at high n in He-like ions, followed by a cascade of decays in which, at X-ray wavelengths, most emission is from $2 \rightarrow 1$ transitions. A detailed analysis was given in Wargelin & Drake (2001).

Charge exchange should equally take place between solar wind ions and neutrals from the interstellar medium streaming into the heliosphere (Cox 1998). By analogy, a similar mechanism is expected for all cool stars with an ionized wind *provided* that the ISM contains a neutral component. Such extended emission could be identified with X-ray spectro-imaging devices (e.g., CCD cameras). Wargelin & Drake (2001) used a parameterized model for the depletion of neutral H near the Sun, depending on the wind mass loss rate, and analyzed (multiple) charge exchange of O^{7+} and O^{8+} to O^{6+} and emission of O VII in the X-ray range. They assumed a spherical, radially expanding wind with a velocity of $v_{\rm ion} = 400$ km s^{-1}. Parameters required in this model are,

- the neutral hydrogen density profile with depletion in the solar vicinity, given by $n_{\rm H}(r) = n_{\rm H_0} \exp^{-\lambda_{\rm H}/r}$ where $\lambda_{\rm H} = 5$ au or 50 au, depending on the mass-loss rate (the higher value being appropriate for a stronger wind). The density at infinity is ~ 0.15 cm^{-3}. This defines the path length for CX, $\lambda_{\rm CX} = (n_{\rm H}\sigma_{\rm CX})^{-1}$, where $\sigma_{\rm CX}$ is the CX cross section between $O^{7+,8+}$ and H, He, or H_2.
- The flux of solar wind O^{7+} and O^{8+} ions is estimated from measurements (3.6×10^{31} O^{8+} and 9.6×10^{31} O^{7+} ions injected into the solar wind per second). The ion

https://doi.org/10.1017/S1743921320001441 Published online by Cambridge University Press

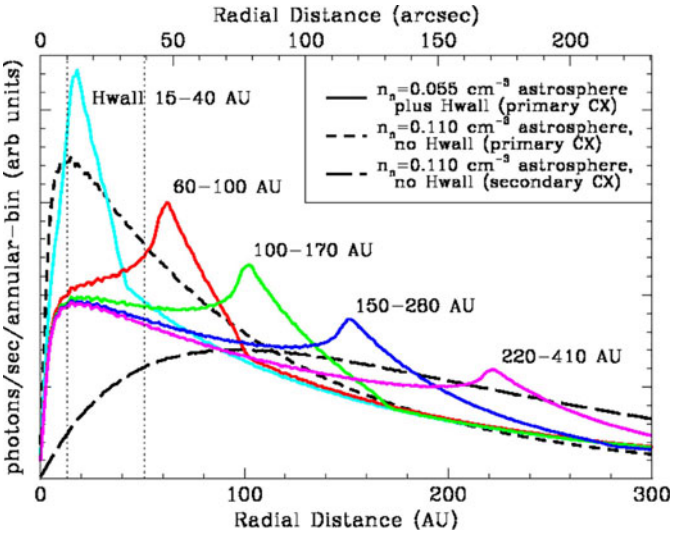

Figure 4. Photon rates in annuli of given radius modeled for CX radiation from the astrosphere around Proxima Centauri, for the *Chandra* ACIS CCD detector. Solid lines are for models with a hemispherical hydrogen wall with twice the ISM neutral density and half the ISM density inside the astrosphere. The short-dashed line refers to models with no hydrogen walls, and a neutral H density equal to the ISM. The long-dashed line is for models also without H walls but for secondary CX emission. (From Wargelin & Drake 2002.)

density profiles with radius follow from two differential equations considering depletion or addition of ions due to CX (at 1 au from the Sun, the *total* ion density is ~ 7 cm^{-3}). The emissivity of CX then is,

$$\epsilon = n_{\rm H} n_{\rm ion} v_{\rm ion} \sigma_{\rm CX}. \tag{4.1}$$

The same authors (Wargelin & Drake 2002) subsequently applied their method to X-ray observations of Proxima Centauri. For this work, they also added a realistic neutral "hydrogen wall" (as discussed in Sect. 3; Fig. 4) to their model of the astrosphere around Prox. Cen. Furthermore, they filtered counts in energy to capture only the CX-line rich region of 453–701 eV. A search for an extended structure at a projected distance of 13–51 au around the star delivered an upper limit translating into an upper limit of $\dot{M} < 3 \times 10^{-13}\ M_\odot$ yr^1 (3σ) or ∼ten times the present-day solar mass-loss rate.

5. Radio Bremsstrahlung from Ionized Stellar Winds

Because winds from cool stars are ionized, they emit bremsstrahlung as a consequence of accelerating/decelerating interactions between electrons and ions. The bremsstrahlung emissivity is a function of electron temperature T and number density $n_{\rm e}$ (absorption coefficient at frequency ν is roughly $\kappa_\nu \propto n_{\rm e}^2\, T^{-3/2}$, therefore emissivity $\eta_\nu \propto n_{\rm e}^2\, T^{-1/2}$). Measuring stellar emission of this type would constitute a direct detection of the winds. This method has indeed been successfully used to quantify wind mass loss rates from massive stars (O, B, and Wolf-Rayet; e.g., Bieging *et al.* 1982; Scuderi *et al.* 1998; Leitherer *et al.* 1995).

The radio free-free flux spectrum for an optically thick, constant-velocity, fully ionized isothermal spherical (isotropic) wind is predicted to be of the form (Panagia & Felli 1975; Wright & Barlow 1975; Olnon 1975)

https://doi.org/10.1017/S1743921320001441 Published online by Cambridge University Press

$$S_\nu = 9 \times 10^{10} \left(\frac{\dot{M}}{v}\right)^{4/3} T^{0.1}\ \nu^{0.6}\ d^{-2}\ \mathrm{mJy}, \tag{5.1}$$

where $\dot{M}$ is the mass loss rate in $M_\odot$ yr^{-1}, T the temperature of the plasma in K, ν the frequency in Hz, v the wind velocity in km s^{-1}, and d the stellar distance in pc. At any frequency one essentially sees emission from gas down to a level where the gas becomes optically thick.

For a wind that is completely optically thin down to the stellar surface, the following spectral flux is observed at Earth:

$$S_\nu = 5 \times 10^{39} \left(\frac{\dot{M}}{v}\right)^{2} T^{-0.35} R_*^{-1} \nu^{-0.1} d^{-2}\ \mathrm{mJy}, \tag{5.2}$$

where R_* is the stellar radius in cm. For non-isothermal winds, the equation of radiative transport must be iterated along all parallel sightlines across the wind region, using the temperature-dependent absorption coefficient.

As for non-isotropic winds, Reynolds (1986) expanded the wind emission theory to a conical pair of collimated polar outflows (analogous to jets). Principally, for the same mass loss rate, wind temperature, and wind velocity as for an isotropic wind, the outflows produce stronger radio emission because of the higher required density.

Searches for wind bremsstrahlung emission were conducted early on, see, e.g., Doyle & Mathioudakis (1991), or Mullan *et al.* (1992). A critical upper limit was obtained by Drake *et al.* (1993) for the wind mass-loss rate of the nearby F5 IV-V star Procyon, namely $\dot{M} < 2 \times 10^{-11}\ M_\odot$ yr^{-1}, an estimate that considered also the *detection* of bremsstrahlung from the chromosphere and optically thick surfaces of active regions, as well as optically thin coronal bremsstrahlung emission. Sensitive millimeter measurements and theoretical arguments have constrained ionized-wind mass loss rates for M dwarfs to $\dot{M} \lesssim$ a few times $10^{-10} M_\odot$ yr^{-1} or $\dot{M} \lesssim 10^{-12} M_\odot$ yr^{-1} (Lim & White 1996; van den Oord & Doyle 1997). Specifically for the nearby Proxima Centauri, Lim *et al.* (1996) derived an upper limit to its mass loss rate of $7 \times 10^{-12} M_\odot$ yr^{-1} for a wind velocity of 300 km s^{-1}, as determined at a wavelength of 3.5 cm.

Gaidos *et al.* (2000) studied wind mass loss evolution of solar analogs to test the hypothesis that the zero-age main-sequence Sun may have been more massive than the present Sun by several percent. This would provide an interesting solution for the "Faint Young Sun Paradox" (FYSP) that confronts evidence of mild climates on early Earth and Mars from geological evidence with the significantly fainter Sun at those times (by 25–30%). Observations of three solar analogs in the age range of 0.3–1.5 Gyr again revealed only flux upper limits down to 12μJy (2σ) at 3.6 cm wavelength, corresponding to mass loss rates of $(4-5) \times 10^{-11} M_\odot$ yr^{-1}. The integrated mass loss rate would be no more than 6% of the solar mass, which however still left the possibility open to explain the FYSP.

Later, deeper observations with the VLA and ALMA of four solar analogs with ages of $\sim 100 - 700$ Myr by Fichtinger *et al.* (2017) again resulted in upper limits down to 9μJy (3σ) at 6–14 GHz wavelengths or detections that were justifiably identified with other emission processes (Fig. 5). These limits, however, were sufficiently low to exclude a higher initial solar mass required to explain the FYSP, with upper limits to a ZAMS mass excess of $\sim 2\%$, based on isotropic winds or polar outflows.

The upper limits for $\dot{M}$ as measured by Gaidos *et al.* (2000) and Fichtinger *et al.* (2017) exceed the expected $\dot{M}$ by about 2 orders of magnitude if a reasonable stellar spin-down/mass-loss evolutionary scenario adapted to the present solar mass-loss rate of $2 \times 10^{-14} M_\odot$ yr^{-1} is assumed (see Sect. 2 above, and Fig. 1 in Gaidos *et al.* 2000).

https://doi.org/10.1017/S1743921320001441 Published online by Cambridge University Press

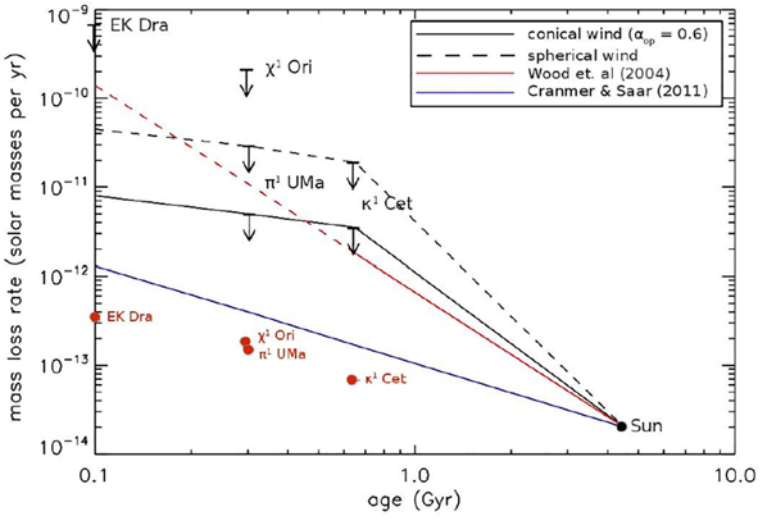

Figure 5. Mass-loss evolution for solar-type stars. The two black solid lines are upper limit estimates for the $\dot{M}$ evolution based on non-detections of stellar wind radio bremsstrahlung (Sect. 5; arrows indicate corresponding $\dot{M}$ upper limits). The upper black dashed line refers to a spherical wind, the lower solid black line to a conical wind with an opening angle of 40 degrees. The red circles are mass-loss estimates from the spin-down model by Johnstone *et al.* (2015) (Sect. 2), while the red line shows the fit from the Lyα absorption model of Wood (2018) (Sect. 3). The blue solid line relates to the theoretical model of Cranmer & Saar (2011). (From Fichtinger *et al.* 2017.)

6. Radio Free-Free Optical Depth of Stellar Winds

The wind bremsstrahlung theory discussed in Sect. 5 can also be used to put limits to the optical depth required by observations of radio emission different from the wind emission. Magnetically active, young stars from spectral type G to M occasionally produce radio flares detected due to their radio gyrosynchrotron emission or a variety of coherent radio emission types. Realistically, these flares take place, like on the Sun, in closed, somewhat compact magnetic loops or loop arcades with heights of a fraction of the stellar radius. Very Long Baseline Interferometry has explicitly supported this picture (e.g., Benz *et al.* 1995; Benz *et al.* 1998), and so has the detection of radio rotational modulation in active stars (Lim *et al.* 1992; Güdel *et al.* 1995).

If the stellar wind became optically thick to radio radiation only a few tenths of a stellar radius above the surface, then radio flares would occur in the optically thick region and therefore not be detectable. Essentially, therefore, the optically thick wind radius should be no larger than the stellar radius, making the wind optically thin (Eq. 5.2). The optically thick radius can be obtained from the (isotropic) wind theory described above, namely

$$R_{\rm thick} = 8 \times 10^{28} \left(\frac{\dot{M}}{v} \right)^{2/3} T^{-0.45} \nu^{-0.7} \ \ {\rm cm}. \tag{6.1}$$

(e.g., Lim & White 1996). Solving this equation for $\dot{M}$ again provides stringent limits to the mass-loss rates of winds given wind temperatures and velocities. Lim & White (1996) obtain $\dot{M} \lesssim 5 \times 10^{-14} - 10^{-12} M_\odot$ yr^{-1} for $v = 300 - 600$ km s^{-1} and wind temperatures of $10^4 - 10^6$ K based on low-frequency observations of flare radio emission from the dMe star YZ CMi.

https://doi.org/10.1017/S1743921320001441 Published online by Cambridge University Press

7. Radio Wave Propagation

Radio waves with a frequency ν propagate through a plasma only if they exceed the local plasma frequency everywhere along the line of sight. Assume a radio point source emitting at frequency ν at a distance of r from the star in a stationary, isothermal wind. The local plasma frequency is

$$\nu_p = \left(\frac{4\pi n_\mathrm{e} e^2}{m_\mathrm{e}}\right)^{1/2} \tag{7.1}$$

where m_e is the mass of the electron and e is the charge of the electron. The condition for a static, isotropic wind is

$$n_\mathrm{i}(r) = \frac{\dot{M}}{4\pi r^2 m_\mathrm{i} v} \ . \tag{7.2}$$

Noting that $n_\mathrm{e} \approx 1.09 n_\mathrm{i}$ and $m_\mathrm{i} \approx 1.25 m_\mathrm{p}$ (m_p being the mass of a proton) for cosmic abundances, we insert Eq. (7.2) into Eq. (7.1) to find

$$\dot{M} < \frac{r^2 m_\mathrm{e} m_\mathrm{i} v \nu_\mathrm{p}^2}{1.09 e^2} \approx 1.2 \times 10^{-58} r^2 v \nu_\mathrm{p}^2 \ M_\odot \ \mathrm{yr}^{-1}. \tag{7.3}$$

For a wind with $v = 400$ km s^{-1} at $r = 10 R_\odot$ and $\nu = 0.1$ GHz, we find a limit of 1.5×10^{15} g s^{-1} $\approx 2.3 \times 10^{-11} M_\odot$ yr^{-1}. Vidotto & Donati (2017) applied this method to potential radio emission of a young Jupiter-mass planet around the T Tauri star V830 Tau (orbital radius 0.057 au). They assumed that the frequency of the planetary radio emission is given by the gyrofrequency determined by the magnetic field strength B in the planetary emission source; they found that $B = 10$ G (corresponding to the gyrofrequency $\Omega_c = 28$ MHz) requires a stellar mass-loss rate of $\dot{M} \lesssim 10^{-10} M_\odot$ yr^{-1}.

The condition $\nu > \nu_\mathrm{p}$ applies to the entire line of sight. For a planet located in the front half of the isotropic stellar wind (e.g., during transit, Fig. 6), the above condition is sufficient because the wind density decreases outward. For locations in the more distant hemisphere, the maximum density along the line of sight must be determined.

8. X-Ray Limits to Stellar Winds

Essentially all cool main-sequence stars host magnetically confined coronae that are detected as variable soft X-rays sources. However, part of the X-ray emission could be due to the hot plasma of a wind that is optically thin to X-rays (like the corona itself).

For a stationary, constant-velocity, spherically symmetric wind, the particle density profile for ions follows Eq. (7.1). The total emission measure of the entire wind is

$$\mathrm{EM} = \int_{R_*}^{\infty} n_e n_i \mathrm{d}V = 1.09 \frac{\dot{M}^2}{4\pi R_* m_\mathrm{i}^2 v^2} \approx 2 \times 10^{46} \frac{\dot{M}^2}{R_* v^2} \tag{8.1}$$

where the factor 1.09 is again the ratio between the electron and ion number densities for a fully ionized plasma with cosmic abundances, and $m_\mathrm{i} \approx 1.25 m_\mathrm{H} \approx 2 \times 10^{-24}$ g.

For a temperature of order ≈ 1 MK, the luminosity of the isothermal wind would be

$$L_\mathrm{X} \approx 10^{-22} \ \mathrm{EM} \tag{8.2}$$

for solar abundances (see, e.g., Audard *et al.* 2004, their Fig. 10). Therefore,

$$\begin{aligned} \dot{M} &\approx 7.1 \times 10^{-13} \left(L_\mathrm{X} R_*\right)^{1/2} v \\ &\approx 3.75 \times 10^{-12} \left(\frac{L_\mathrm{X}}{10^{27} \ \mathrm{erg/s}}\right)^{1/2} \left(\frac{v}{400 \ \mathrm{km/s}}\right) \left(\frac{R_*}{7 \times 10^{10} \ \mathrm{cm}}\right)^{1/2} M_\odot/\mathrm{yr} \end{aligned} \tag{8.3}$$

https://doi.org/10.1017/S1743921320001441 Published online by Cambridge University Press

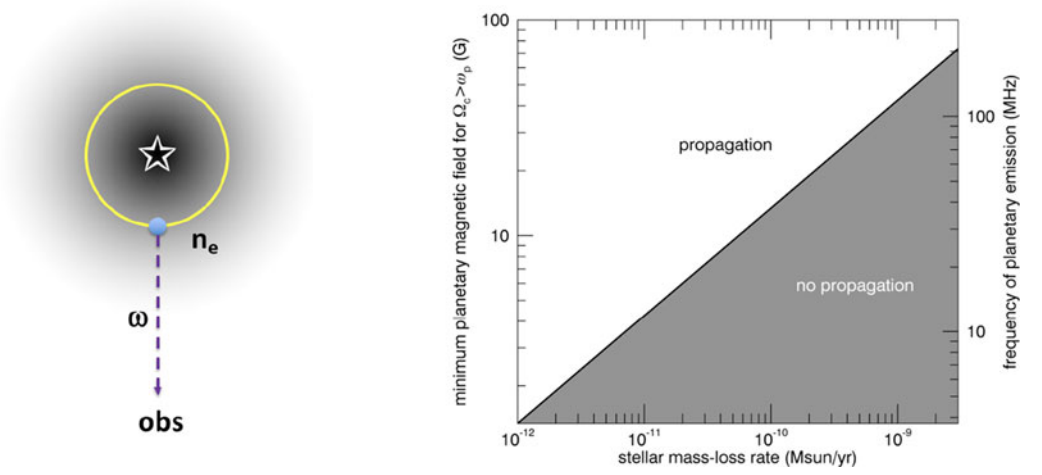

Figure 6. *Left:* Sketch illustrating a stellar wind with decreasing density outwards, and a planet orbiting in the wind where the wind density is n_e. The angular frequency ω must exceed the local plasma frequency ω_p along the entire line of sight. – *Right:* Minimum planetary magnetic field intensity required for the propagation of planetary radio emission through the wind of the host star as a function of stellar wind mass-loss rate, assuming that the planetary emission takes place at the gyrofrequency in the planetary magnetic field emission source (see right y axis). The shaded area is for parameter combinations that do not allow planetary radio emission to propagate through the wind. (Right figure from Vidotto & Donati 2017.)

For $L_X = 10^{27} - 10^{30}$ erg s^{-1} for a solar analog and $v = 400$ km s^{-1}, the maximum mass-loss rate (assuming that all observed X-ray emission is due to a wind) would be $3.75 \times 10^{-12} - 1.2 \times 10^{-10}$ $M_\odot$ yr^{-1}. This obviously does not apply to the Sun where almost all X-ray emission is from closed active regions and the measured wind mass-loss rate is $\sim 2-3$ orders of magnitude lower than from the above estimate, but these limits provide conservative constraints to the total mass loss rate from hot ionized winds (note that most of the wind radiation originates from close to the stellar surface where the temperatures are still high, because of the r^{-2} dependence of the density).

An estimate for the maximum possible wind mass loss rate for Proxima Centauri based on the X-ray luminosity was briefly mentioned by Lim & White (1996), with $\dot{M} \lesssim 6 \times 10^{-11} M_\odot$ yr^{-1} for the active mid-M dwarf YZ CMi. In general for mid M dwarfs with $L_X = 10^{26} - 10^{29}$ erg s^{-1} and a radius of $\approx 0.4 R_\odot$, one finds a maximum of $\dot{M} = 7.5 \times 10^{-13} - 2.4 \times 10^{-11}$ $M_\odot$ yr^{-1}.

9. Wind-Planet Interactions

Planets with atmospheres interact in various ways with stellar winds. For example, stellar winds can drag ions formed in the upper atmospheres of planets. Stellar winds also transport shock fronts from coronal mass ejections and high-energy particles produced in those shocks or in stellar flares. Such particles can interact with planetary atmospheres where they induce sputtering, ionization, and drive chemical reactions (see, for example, Lammer *et al.* 2003; Airapetian *et al.* 2016). The collision between the wind and a planetary magnetosphere may also form a detectable shock in front of the planet (Vidotto *et al.* 2011a). There is a rapidly increasing amount of literature modeling stellar wind parameters based on exoplanetary observations. I briefly discuss four exemplary cases in this section.

https://doi.org/10.1017/S1743921320001441 Published online by Cambridge University Press

Vidotto *et al.* (2010) studied a model of a bow shock forming as a planet moves in, and collides with, the stellar wind. Specifically, the early ingress of the transiting planet WASP-12b in orbit around the late-F-type main-sequence star WASP-12 requires an absorbing column density for Mg of $> 1.4 \times 10^{13}$ cm^{-2} (Lai *et al.* 2010), corresponding to a shock density of $n_{\rm H} \approx 6 \times 10^6$ cm^{-3} or a pre-shock wind density of $n_{\rm obs} \approx 1.5 \times 10^6$ cm^{-3} at the location of the planet with an orbital radius of $3.15 R_*$. The coronal temperature must be $< 4.2 \times 10^6$ K to allow a shock to form. The wind velocity at the planet's position is a function of the wind temperature, which is unknown, but if known, would then allow us to calculate $\dot{M}$ from $n_{\rm obs}$ and the velocity.

Observations of Lyα excess absorption profiles (also discussed in the context of astrospheric H walls in Sect. 3) including inflated planetary hydrogen atmospheres in transit around the host star HD 209458 were presented by Ben-Jaffel (2007). Line modeling was presented in various publications, but Kislyakova *et al.* (2014) was the first to develop a model including all relevant physical effects, namely, i) Lyα radiation pressure, ii) natural line broadening, iii) line broadening due to the velocity distribution of particles along the line of sight, iv) photoionization, v) electron impact ionization, and vi) exospheric energetic charge exchange to form energetic neutral atoms. These authors find an extended H corona around the planet arranged in the shape of a cometary tail in the stellar wind and best-fit parameters for the Lyα profile of 400 km s^{-1} for the wind velocity, a wind particle density of 5×10^3 cm^{-3}, and therefore, using the orbital distance of 0.047 au, a mass-loss rate of $\dot{M} = 4 \times 10^{-14}$ $M_\odot$ yr^{-1} for this F9 V star.

Lecavelier des Etangs *et al.* (2012) estimated wind density and velocity for the planet host HD 189733 (K2 V) from the transit Lyα profile, using an N-body simulation of the upper atmospheric H atoms that interact with the wind and are subject to radiation pressure and charge exchange. The best-fit model parameters include the wind temperature $T \approx 10^5$ K, the wind density $n = 3 \times 10^3$ cm^{-3}, and the wind velocity $v = 190$ km s^{-1}. Given the orbital radius of the planet of 0.031 au, one finds $\dot{M} \approx 5 \times 10^{-15}$ $M_\odot$ yr^{-1}, which is 4 times less than the present-day solar wind.

Along similar lines, Vidotto & Bourrier (2017) modeled the interaction between the wind of the M2.5 dwarf GJ 436 and the warm Neptune GJ 436b. The model is a spherically symmetric, steady-state isothermal wind. The best-fit model indicates a wind temperature of 0.41 MK, a terminal velocity of 370 km s^{-1}, a local wind velocity of 85 km s^{-1} as the wind is still accelerating at the position of the close-in planet (orbital radius 0.029 au), and a local proton density of 2×10^3 cm^{-3}. This implies $\dot{M} \approx 1.2^{+1.3}_{-0.75} \times 10^{-15}$ $M_\odot$ yr^{-1}, or 0.059 times the present solar mass-loss rate.

10. Slingshot Prominences

Apart from a steady wind, mass may also be lost in episodic ejections, in the case discussed here in prominences. The presence of co-rotating, relatively cool material trapped in coronal magnetic fields has been demonstrated spectroscopically in Hα absorption transients in active, rapidly rotating stars (Collier Cameron & Robinson 1989). Cool prominences can form in the apex region of coronal magnetic loops when a thermal instability occurs. The drop in pressure will attract more material from below.

To analyze the situation further, Jardine & Collier Cameron (2019) distinguish three coronal regions: i) the region from the stellar surface up to the sonic radius R_s where the wind speed is equal to the sound speed. ii) The region between R_s and the Alfvén radius $R_{\rm A}$ where the wind speed reaches the Alfvén speed, and iii) the region beyond $R_{\rm A}$. Coronal magnetic loops can be closed in regions (i) and (ii), but are open in region (iii). Assuming that the condensations form easiest if the loop apex is at the co-rotation radius $R_{\rm K}$, what then matters is the location of $R_{\rm K}$ relative to the above three regions. Note that $R_{\rm K}$ increases with increasing Ω, like $R_{\rm K} = (GM_*/\Omega^2)^{1/3}$.

https://doi.org/10.1017/S1743921320001441 Published online by Cambridge University Press

If a loop-top coronal condensation (i.e., at $R_{\rm K}$) lies below R_s, then the loop can remain hydrostatic and a hydrostatic equilibrium can always be established (hydrostatic regime). If the condensation (at $R_{\rm K}$) forms in a loop apex above R_s, then cooling material accumulates because the flow arrives supersonically in that region and hydrostatic equilibrium in the entire loop cannot be established. The increasing pressure will eventually release the prominence, and depending on whether it is below or above the co-rotation radius, it will fall back to the star or will be episodically ejected (limit-cycle regime). If the coronal condensation (at $R_{\rm K}$) forms beyond the Alfvén radius, then it will not accumulate further mass but will flow out along the open field lines (open regime).

The analysis by Jardine & Collier Cameron (2019) relies on the assumption that the coronal filling acts like a wind, and for this the plasma electron temperature matters because R_s is a function of T, $R_s = GM_*/2c_s^2$. The temperature required such that $R_s = R_{\rm K}$ is,

$$T_{\rm crit} = 1.6 \times 10^6 \ {\rm K} \left(\frac{M_*}{M_\odot}\right)^{2/3} \left(\frac{P}{1 \ {\rm d}}\right)^{-2/3}. \tag{10.1}$$

The expected average wind mass-loss rate in particular from the episodic ejections from the limit-cycle regime where $R_s < R_{\rm K} < R_{\rm A}$ follows from observations. The observed masses $m_{\rm p}$ and lifetimes τ of Hα prominences provide an average mass-upflow rate into the prominence,

$$\dot{m}_{\rm p} \approx \frac{m_{\rm p}}{\tau}. \tag{10.2}$$

The footpoint area of the respective loop can be estimated from the dipole approximation,

$$A_0 = A_{\rm p} \left(\frac{R_*}{R_{\rm p}}\right)^3 \tag{10.3}$$

where $R_{\rm p}$ is the radial height of the prominence, and $A_{\rm p}$ is the cross-section area of the prominence in the loop. Then, assuming full coverage of the star with this type of wind, the wind mass-loss rate will be

$$\dot{M} = \frac{4\pi R_*^2}{2A_0} \dot{m}_{\rm p} \approx 100 \frac{m_{\rm p}}{\tau}. \tag{10.4}$$

Some $\dot{M}$ estimates for very rapidly rotating, active stars are shown in Fig. 7. The highest mass-loss rates reach up to 3000 times the solar rate per unit area and suggest that the correlation found by Wood *et al.* (2005), Eq. (3.1), continues to hold approximately toward much more active stars, and there may be no breakdown of $\dot{M}$ at some specific activity level.

11. Accretion Contamination in White Dwarf Atmospheres

In white dwarfs (WD), heavy elements are supposed to settle below the upper atmosphere on time scales $\lesssim 10^6$ yr, giving rise to pure H or He photospheres. Nevertheless, several white dwarfs with long cooling times show spectroscopic evidence of heavy metals in their atmospheres. The common explanation for this metal contamination is accretion of solar-abundance material from the interstellar medium. However, as discussed in Debes (2006), close WD + M dwarf binaries show heavy metals anomalously often. The idea is that the contaminating material in the WD originates from the stellar wind of the companion red dwarf through Bondi-Hoyle accretion. In this case, the accretion rate is,

$$\dot{M}_{\rm acc} = \frac{4\pi G^2 M_{\rm WD}^2 \rho(R)}{v_{\rm rel}^3} \tag{11.1}$$

https://doi.org/10.1017/S1743921320001441 Published online by Cambridge University Press

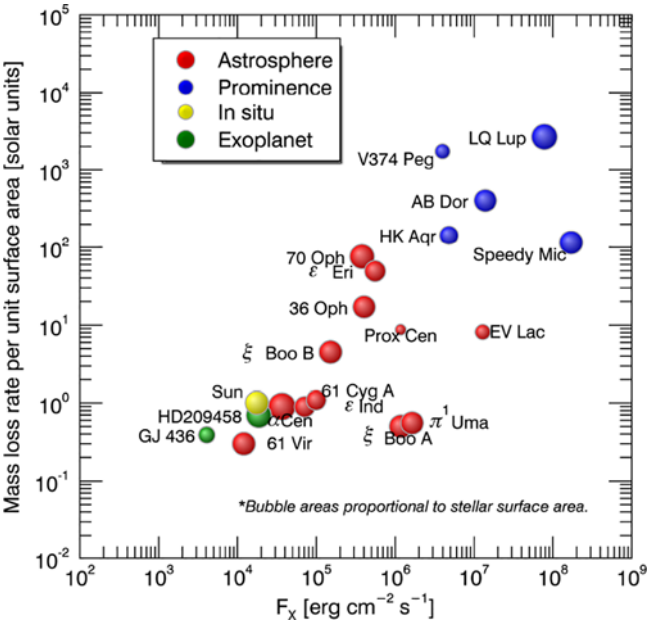

Figure 7. Stellar mass-loss rate per unit surface area plotted against the X-ray surface flux. The blue dots are for stars interpreted with the slingshot prominence method (Sect. 10). Red dots are from the astrospheric Lyα method (Sect. 3; see also Fig. 3). The green dots use exoplanetary atmospheres (Sect. 9). (From Jardine & Collier Cameron 2019.)

(Bondi & Hoyle 1944; see Debes 2006) where G is the gravitational constant, $M_{\rm WD}$ is the mass of the white dwarf, $\rho(R)$ is the density of the M dwarf wind at the position of the accreting WD (distance of R), and $v_{\rm rel}$ is the relative velocity between the WD and the wind flow, composed of the radial wind velocity and the WD orbital velocity. In an assessment presented by Debes (2006), the wind speed is assumed to be the escape speed of the M dwarf, which is approximately true also for the Sun, although physical drivers for the wind velocity (coronal heating) should make this only a rough approximation.

The convective atmosphere collects heavy elements by accretion while these elements subsequently diffuse below the convection zone. These two competing mechanisms should be in a steady-state equilibrium. Using Ca as an easily observable element, the accretion rate of Ca is (see Debes 2006)

$$\dot{M}_{\rm acc,Ca} = \dot{M}_{\rm acc}[{\rm Ca/H}]_{\odot} \tag{11.2}$$

where the solar abundance of Ca has been assumed for the accreting material from the M dwarf wind. The rate of diffusion of Ca out of the convection zone is,

$$\dot{M}_{\rm diff,Ca} = \frac{qM_{\rm WD}}{\tau}[{\rm Ca/H}] \tag{11.3}$$

where $M_{\rm WD}$ is the WD mass, q is the fractional mass in the convection zone and the photosphere, and τ is th diffusion time scale. The Ca abundance is [Ca/H], as observed. We assume a spherical, stationary wind for the M dwarf with a rate $\dot{M}$, so that the density at a distance R is

$$\rho(R) = \frac{\dot{M}}{4\pi R^2 v}. \tag{11.4}$$

https://doi.org/10.1017/S1743921320001441 Published online by Cambridge University Press

Table 1. Summary of methods for wind mass-loss rate measurements

Method	Type	Caveats
Spin-down	indirect	torque formula
H walls, Lyα	indirect	hydrodynamic model, presence of neutral ISM
Astrospheric CX	direct	presence of neutral ISM
Radio bremsstrahlung	direct	other radio emission; wind temperature and velocity
Radio free-free absorption	direct	presence coronal emission; wind temperature and velocity
Radio wave propagation	indirect	planetary magnetic field strength and radio emission
X-ray emission	direct	assumed wind temperature; stellar X-rays
Planetary Lyα absorption	indirect	model, planetary atmosphere
White dwarf metal contamination	indirect	orbital separation, wind velocity, diffusion parameters

Requiring $\dot{M}_{\rm acc,Ca} = \dot{M}_{\rm diff,Ca}$ leads to

$$\dot{M}_{\rm acc} = \frac{qM_{\rm WD}}{\tau}\frac{[{\rm Ca/H}]}{[{\rm Ca/H}]_\odot} \tag{11.5}$$

(Debes 2006). Since this must be the same as Eq. (11.1) (assuming v for $v_{\rm rel}$), we find

$$\dot{M} = \frac{q}{\tau}\frac{[{\rm Ca/H}]}{[{\rm Ca/H}]_\odot}\frac{R^2v^4}{G^2M_{\rm WD}}\ . \tag{11.6}$$

This method for $\dot{M}$ has a number of caveats, most importantly the poorly known R (if the orbit orientation and orbit eccentricity are not known), the assumption of the wind velocity, and the uncertainties in the calculated parameters q and τ. Debes (2006) suggests that the estimates are good to about one order of magnitude for close binaries. He presents three such cases, all of which show very low $\dot{M}$ in the range $\dot{M} \approx 10^{-16} - 6 \times 10^{-15}\ M_\odot\ {\rm yr}^{-1}$ for M dwarf masses of $0.095 - 0.36\ M_\odot$ (spectral types ~M4–6.5) and orbital separations ≤ 0.015 au. These $\dot{M}$ values are much lower than $\dot{M}_\odot$. Even lower values are reported by Parsons *et al.* (2012) and references therein.

12. Discussion and Conclusions

The previous sections have summarized a variety of methods presently available to infer the presence of stellar mass loss, and in many cases provide estimates or upper limits for $\dot{M}$. The methods can be grouped into *direct* or *indirect* methods. Table 1 summarizes the methodologies and caveats. The latter refer to those issues that are poorly known or that are difficult to isolate from the wind signatures.

Direct wind measurements rely on electromagnetic emission of the wind plasma itself, or optical-depth related absorption or attenuation processes in the wind plasma. This category comprises measurements of radio bremsstrahlung, radio optical depth of the wind plasma to other stellar radio emission, radio wave propagation effects near the plasma frequency, X-ray thermal emission from the wind, and X-ray emission due to charge exchange between wind ions and neutrals penetrating into the astrosphere from the ISM. While these measurements are based on straightforward interpretation of observational data, emission and absorption effects in ionized stellar winds have turned out to be weak so that essentially all observations have provided upper limits to $\dot{M}$. This is not by itself a weakness. Stringent upper limits help constrain stellar mass-loss models; they have also rejected a model in which a significantly more massive young Sun helps solve the Faint Young Sun Paradox. Most direct methods suffer, however, from competing radiation from the star itself. This is particularly true for coronal X-rays outshining the feeble astrospheric charge exchange radiation, or for wind radio bremsstrahlung in the presence of chromospheric radio emission if the wind is optically thin.

https://doi.org/10.1017/S1743921320001441 Published online by Cambridge University Press

Table 2. Selected published estimates of $\dot{M}$ using different methodologies

Method	$\dot{M}$ (F/G/K Dwarfs) $[M_\odot\ \mathrm{yr}^{-1}]$	$\dot{M}$ (M Dwarfs) $[M_\odot\ \mathrm{yr}^{-1}]$	References[1]
Spin-down	$10^{-14} - 4 \times 10^{-13}$	$10^{-14} - 10^{-13}$	1
H walls, Lyα	$< 10^{-15} - 2 \times 10^{-12}$	$< 2 \times 10^{-15}$	2
Astrospheric CX	...	$< 3 \times 10^{-13}$	3
Radio bremsstrahlung	$< (2-3) \times 10^{-11}$ [2]	$< (6-9) \times 10^{-10}$, $< 7 \times 10^{-12}$	4
Radio free-free absorption	$< 7 \times 10^{-10}$	$< 5 \times 10^{-14} - < 10^{-11}$	5
Radio wave propagation	$< 10^{-10}$	...	6
X-ray emission	$< 3.5 \times 10^{-12} - < 10^{-10}$	$< 7 \times 10^{-13} - < 2 \times 10^{-11}$	7
Planetary Lyα absorption	$5 \times 10^{-15} - 4 \times 10^{-14}$	1.2×10^{-15}	8
White dwarf metal contamination	...	$10^{-16} - 6 \times 10^{-15}$	9

Notes: [1]References: 1: Johnstone *et al.* (2015); 2: Wood (2004); 3: Wargelin & Drake (2002); 4: Fichtinger *et al.* (2017) (G dwarfs), Lim & White (1996) (M dwarfs AD Leo, YZ CMi), Lim *et al.* (1996) Prox. Cen. ($< 7 \times 10^{-12}$); 5: Fichtinger *et al.* (2017) (G dwarfs), Lim & White (1996) (M dwarf YZ CMi); 6: Vidotto & Donati (2017) (V830 Tau, T Tauri star); 7: this paper, Sect. 8. 8: Lecavelier des Etangs *et al.* (2012) for HD 189733 (K2 V), Kislyakova *et al.* (2014) for HD 209458 (F9 V), Vidotto & Bourrier (2017) for GJ 436 (M2.5); 9: Debes (2006), also lower values in Parsons *et al.* (2012).

[2]Only for spherical winds; lower upper limits possible for conical winds.

Indirect wind measurements use features for which the wind is responsible but that themselves are distinct from the wind. This category comprises the inference of stellar winds from stellar rotation and evolutionary spin-down, interpretation of Lyα line absorption in the hydrogen walls around astrospheres embedded in a partially neutral ISM, inferences for the stellar wind from observations of planetary atmospheres, the interpretation of slingshot prominences in very active stars, and white dwarf metal contamination in WD + M dwarf close binaries. These methods have the advantage of using features that often "amplify" the evidence of a wind. The difficulty with these methods comes from the need of complex models relating the observed features to the putative stellar winds. Nevertheless, indirect measurements have been more successful in providing estimates for $\dot{M}$ rather than upper limits even though model limitations need to be kept in mind (e.g., the breakdown of the $\dot{M}$ relation from Lyα absorption toward very active stars, or the relation between $\dot{M}$ and the angular momentum loss rate based on a "torque formula" for stellar spin-down).

Table 2 summarizes some select results from various methods. Of course, these results by now means cover a representative parameter range of stars as the observed targets are biased by target selection criteria. There is need to infer $\dot{M}$ from different methods in the hope to cross-calibrate them and verify their applicability. This has succeeded only very rarely. I mention the measurements of $\dot{M}$ using Lyα absorption, astrospheric CX, X-ray thermal emission, and radio bremsstrahlung for Proxima Centauri or Lyα absorption and stellar spin-down estimates for the solar analog π^1 UMa. In the former case, the measurements are in agreement with each other although three of them (X-ray thermal emission, radio bremsstrahlung and astrospheric CX) provided only upper limits. For π^1 UMa, in contrast, the two estimates contradict each other, as spin-down requires strong winds while the Lyα method delivered an estimate of $\dot{M}$ even below the present-day solar value. This clearly illustrates the need for further multiple $\dot{M}$ measurements.

These reservations and caveats aside, observations in the past two decades have started confining wind mass loss for cool main-sequence stars to levels that look reasonable in the context of the solar $\dot{M}$ and spin-down evolution, with results or upper limits that straddle around the solar value up to values 100–1000 times the solar $\dot{M}$ for very active stars. This can be compared to the stellar X-ray luminosities that vary in a similar range.

https://doi.org/10.1017/S1743921320001441 Published online by Cambridge University Press

Acknowledgments

It is pleasure to thank the organizers for a wonderful conference and for giving me the opportunity to present this review. This research has been supported by the Austrian Science Fund FWF through project S116 *Pathways to Habitability: From Disks to Active Stars, Planets and Life* and the related subproject S11604 *Radiation & Wind Evolution from the T Tauri Phase to ZAMS and Beyond.*

References

Airapetian, V. S., Glocer, A., Gronoff, G., *et al.* 2016, *Nature Geosci.*, 9, 452
Audard, M., Telleschi, A., Güdel, M., *et al.* 2004, *ApJ*, 617, 531
Ayres, T. R. 1997, *J. Geophys. Res.*, 102, 1641
Ben-Jaffel, L. 2007, *ApJ*, 671, L61
Benz, A. O., Alef, W., Güdel, M. 1995, *A&A*, 298, 187
Benz, A. O., Conway, J., Güdel, M. 1998, *A&A*, 331, 596
Bieging, J. H., Abbott, D. C., Churchwell E. B. 1982, *ApJ*, 263, 207
Biermann, L., 1951, *ZfA*, 29, 274
Bondi, H., Hoyle, F. 1944, *MNRAS*, 104, 273
Collier Cameron, A., Robinson, R. D., 1989, *MNRAS*, 238, 657
Cox, D. P. 1998, in The Local Bubble and Beyond, ed. D. Breitschwerdt, M. J. Freyberg, & J. Trümper (Berlin: Springer), 121
Cravens, T. E. 1997, *Geophys. Res. Lett.*, 24, 105
Cranmer, S. R., Saar, S. H. 2011, *ApJ*, 741, 54
Debes J. H., 2006, *ApJ*, 652, 636
Doyle, J. G., Mathioudakis, M. 1991, *A&A* 241, L41
Drake, S. A., Simon, T., & Brown, A. 1993, *ApJ*, 406, 247
Fichtinger, B., Güdel, M., Mutel, R. L., *et al.* 2017, *A&A*, 599, A127
Gaidos, E. J., Güdel, M., Blake, G. A. 2000, *Geophys. Res. Lett.*, 27, 501
Gallet, F., Bouvier, J. 2013, *A&A*, 556, A36
Gayley, K. G., Zank, G. P., Pauls, H. L., Frisch, P. C., Welty, D. E. 1997, *ApJ*, 487, 259
Güdel, M., Schmitt, J. H. M. M., Benz, A. O., Elias, II, N. M. 1995, *A&A*, 301, 201
Holzwarth, V., Jardine, M. 2007, *A&A*, 463, 11
Irwin, J., Berta, Z. K., Burke, C. J., *et al.* 2011, *ApJ*, 727, 56
Jardine, M., Collier Cameron, A. 2019, *MNRAS*, 482, 2853
Johnstone, C. P., Güdel, M., Brott, I., Lüftinger, T. 2015, *A&A*, 577, A28
Kislyakova, K. G., Holmström, M., Lammer, H., *et al.* 2014, *Science*, 346, 981
Kraft, R. P. 1967, *ApJ*, 150, 551
Lai, D., Helling, C., van den Heuvel, E. P. J. 2010, *ApJ*, 721, 923
Lammer, H., Lichtenegger, H. I. M., Kolb, C., *et al.* 2003, *Icarus*, 165, 9
Lecavelier des Etangs, A., Bourrier, V., Wheatley, P. J., *et al.* 2012, *A&A*, 543, L4
Leitherer, C., Chapman, J. M., Koribalski, B. 1995, *ApJ*, 450, 289
Lim, J., White, S. M. 1996, *ApJ*, 462, L91
Lim, J., Nelson, G. J., Castro, C., *et al.* 1992, *ApJ*, 388, L27
Lim, J., White, S. M., Slee, O. B. 1996, *ApJ*, 460, 976
Linsky, J. L., Wood, B. E. 1996, *ApJ*, 463, 254
Lisse, C. M., Dennerl, K., Englhauser, J., *et al.* 1996, *Science*, 274, 205
Matt, S. P., MacGregor, K. B., Pinsonneault, M. H., Greene, T. P. 2012, *ApJ*, 754, L26
Matt, S. P., Brun, A. S., Baraffe, I., *et al.* 2015, *ApJ*, 799, L23
McComas, D. J., Alexashov, D., Bzowski, M., *et al.* 2012, Science, *336*, 1291
Mullan, D. J., Doyle, J. G., Redman, R. O., Mathioudakis M. 1992, *ApJ*, 397, 225
Olnon, F. M. 1975, *A&A*, 39, 217
Parker, E. N. 1958, *ApJ*, 128, 664
Panagia, N. & Felli, M. 1975, *A&A*, 39, 1
Parsons S. G. Marsh, T. R., Gänsicke, P. T. *et al.* 2012, *MNRAS*, 420, 3281

Reynolds, S. P. 1986, *ApJ*, 304, 713
Scuderi, S., Panagia, N., Stanghellini, C., *et al.* 1998, *A&A*, 332, 251
Skumanich, A. 1972, *ApJ*, 171, 565
Soderblom, D. R., Stauffer, J. R., MacGregor, K. B., Jones, B. F. 1993, *ApJ*, 409, 624
Stone, E. C., Cummings, A. C., McDonald, F. B., *et al.* 2008, *Nature*, 454, 71
Stone, E. C., Cummings, A. C., Heikkila, B. C., Lal, N. 2019, *Nature Astron.*, 3, 1013
Tu, L., Johnstone, C. P., Güdel, M., Lammer, H. 2015, *A&A*, 577, L3
van den Oord, G. H. J., Doyle, J. G. 1997, *A&A* 319, 578
Vidotto, A. A., Donati, J.-F. 2017, *A&A*, 602, A39
Vidotto, A. A., Bourrier, V. 2017, *MNRAS*, 470, 4026
Vidotto, A. A., Jardine, M., Helling, Ch. 2011a, *MNRAS*, 414, 1573
Vidotto, A. A., Jardine, M., Opher, M. *et al.* 2011b, *MNRAS*, 412, 351
Vidotto, A. A., Jardine, M., Helling, Ch. 2010, *ApJ*, 722, L168
Vidotto, A. A., Gregory, S. G., Jardine, M., *et al.* 2014, *MNRAS*, 441, 2361
Wargelin, B. J., Drake, J. J. 2001, *ApJ*, 546, L57
Wargelin, B. J., Drake, J. J. 2002, *ApJ*, 578, 503
Weber, E. J., Davis, Jr., L. 1967, *ApJ*, 148, 217
Wood, B. E. 2004, *Liv. Rev. Solar Phys.*, 1, id. 2
Wood, B. E., Müller, H.-R., Zank, G. P., *et al.* 2005, *ApJ*, 628, L143
Wood, B. E. 2018, in Dissipative and Heating Processes in Collisionless Plasma: The Solar Corona, the Solar Wind, and the Interstellar Medium, IOP J. Phys. Conf. Ser. 1100, 012028
Wright, A. E., Barlow, M. J. 1975, *MNRAS*, 170, 41

Discussion

HAN: In order to get the mass-loss rate, we need to know the torque in the spin-down method. The torque is inferred from a hydro simulation. How reliable is this simulation? What are the uncertainties in the simulation?

GÜDEL: Johnstone *et al.* (2015) used a specific torque formula from simulations performed by Matt *et al.* (2012). This formula (simplified above in Eq. 2.1) derives from 2D axisymmetric MHD simulations using a dipolar stellar magnetic field. The latter assumption is a first approximation because the largest-scale structure of the field is dominated by the dipolar component. As the authors mention, the formula is invalid in the limit of very weak magnetic fields, because other, e.g., viscous, effects begin to be more important. Then, the wind-driving physics, such as the coronal temperature and the heating and cooling physics, is poorly understood. The authors estimate a factor of 2 uncertainty coming from these sources. Furthermore, these simulations assumed a dipole magnetic field that is aligned with the stellar rotation axis. For a pure quadrupolar field with the same surface magnetic field strength, however, the torque would be reduced by a factor of ten! Newer torque calculations for example by Matt *et al.* (2015) still show disagreements with observations of low-mass slow rotators. Johnstone *et al.* (2015) aimed at fitting observed rotation distributions and therefore used a "fudge" factor in Matt et al.'s torque formula to include all ignored unknown physics; this factor is derived from requiring the torque to lead to the known spin-down rate for old solar-type stars (age $\sim 1-5$ Gyr) assuming the present-day average magnetic field and the present-day solar mass-loss rate; these assumptions are again somewhat uncertain as the state of activity of the Sun may significantly vary on time scales shorter than the general evolutionary time scales (but still on time scales $\gg$ the activity cycle time scale). But introducing such an empirical fit parameter should at least reduce the systematic – and potentially large – uncertainties due to ignored physics in the models.

https://doi.org/10.1017/S1743921320001441 Published online by Cambridge University Press